Using 5D Flow MRI to Decode the Effects of Rhythm on Left Atrial 3D Flow Dynamics in Patients with Atrial Fibrillation

Liliana Ma[1,2], **Jérôme Yerly**[3,4], **Lorenzo Di Sopra**[3], **Davide Piccini**[3,5], **Jeesoo Lee**[1], **Amanda DiCarlo**[1], **Rod Passman**[6], **Philip Greenland**[6], **Daniel Kim**[1,2], **Matthias Stuber**[3,4], **Michael Markl**[1,2]

[1]Department of Radiology, Feinberg School of Medicine, Chicago, IL, USA [2]Department of Biomedical Engineering, Northwestern University, Evanston, IL, USA [3]Department of Diagnostic and Interventional Radiology, Lausanne University Hospital (CHUV) and University of Lausanne (UNIL), Switzerland [4]Center for Biomedical Imaging (CIBM), Lausanne, Switzerland [5]Advanced Clinical Imaging Technology, Siemens Healthcare AG, Lausanne, Switzerland [6]Department of Medicine and Preventive Medicine, Feinberg School of Medicine, Chicago, IL, USA

Abstract

Purpose: This study used a 5D flow framework to explore the influence of arrhythmia on thrombogenic hemodynamic parameters in patients with atrial fibrillation (AF).

Methods: A fully self-gated, 3D radial, highly-accelerated free-running 5D flow sequence with interleaved 4-point velocity-encoding was acquired using an in vitro arrhythmic flow phantom and in 25 patients with a history of AF (68±8y, 6F). Self-gating signals were used to calculate AF burden, bin data, and tag each k-space line with its RR_{Length}. Data were binned as an RR-resolved dataset with 4 RR-interval bins (RR1-RR4, short-to-long) for compressed sensing reconstruction. AF burden was calculated as interquartile range of all intrascan RR-intervals divided by median RR-interval, and left atrial (LA) stasis as the percent of the cardiac cycle where the velocity was <0.1 m/s.

Results: In vitro results demonstrated successful recovery of RR-binned flow curves using RR-resolved 5D flow compared to a real-time PC reference standard. In vivo, 5D flow was acquired in 8:48 minutes. AF burden was significantly correlated with 5D flow-derived peak (PV) and mean (MV) velocity and stasis ($|\rho|$=0.54-0.75, p<0.001). Sensitivity analyses determined a threshold for low versus high AF burden at 9.7%. High burden patients had increased LA mean stasis (up to +42%, p<0.01), and lower MV and PV (−30%, −40.6%, respectively, p<0.01). RR4 deviated furthest from respiratory-resolved reconstruction (end-expiration) with increased mean stasis (7.6%±14.0%, p=0.10) and decreased PV (−12.7±14.2%, p=0.09).

Conclusions: RR-resolved 5D flow can capture temporal and RR-resolved 3D hemodynamics in <10 minutes and offers a novel approach to investigate arrhythmias.

Name and complete address of correspondence: Liliana Ma, PhD, Address: 737 N Michigan Avenue Suite 1600, Chicago, IL, 60611, liliana.ma@northwestern.edu.

Introduction

Atrial fibrillation (AF) is the most common sustained cardiac arrhythmia, affecting over 33 million patients worldwide and becoming increasingly prevalent with the aging population. [1-5] AF is associated with increased risk of ischemic stroke,[6] attributed to thromboembolism originating in the left atrium (LA) and particularly in the left atrial appendage (LAA). Changes in LA/LAA hemodynamics (low peak emptying velocities and increased flow stasis) in AF have been associated with thromboembolism formation and thus stroke risk.[7] However, these studies have primarily employed transesophageal echocardiography, which is semi-invasive, may require sedation, and cannot capture the complex 3D flow dynamics inside the LA and LAA.

As an alternative, 4D flow MRI has been used for comprehensive evaluation of 3D hemodynamics in the left atrium in a number of prior studies.[8-12] These studies have found that patients in AF have significantly increased LA and LAA stasis and decreased peak velocities (PV), factors associated with an increased propensity for atrial thrombogenesis, compared to control populations.[13] However, current techniques are suboptimal in this context, as 4D flow techniques average data over multiple heart cycles, which prevents investigation of the effects of arrhythmic heartbeats and variable RR-interval on atrial flow characteristics. Recent explorations into multi-dimensional and self-gated imaging have pushed the boundaries of "conventional" cardiac imaging towards more efficient scan times and operator ease-of-use.[14-24]

Recently, a fully self-gated free-running 5D flow framework was introduced.[19,21,23,25,26] This framework featured a continuous, free-running, 3D radial sequence, with interleaved 3-directional velocity encoding as well as inherent self-gating projections to encode cardiac and respiratory motion without external gating signals.[21] The self-gating signal was used to retrospectively bin the flow-encoded three-dimensional data of the heart into cardiac-temporal (4th dimension) and respiratory-resolved (5th dimension) bins. A subsequent multidimensional compressed sensing (CS) reconstruction was employed to calculate the final 5D flow data (5D = 3D + time + respiration). In this study, we have adapted this 5D flow framework and used the 5th dimension (previously respiration) to capture different RR-interval durations in AF patients with arrhythmic heart rates. Our goal was to validate this 5D flow RR-resolved framework (RR-resolved 5D flow) in vitro in a dedicated arrhythmic pulsatile phantom experiment and to apply it to a cohort of patients with AF to systematically explore the influence of arrhythmic heart rates on left atrial thrombogenic hemodynamic parameters. We hypothesized that RR-resolved 5D flow would be able to detect RR-interval-driven variations in LA hemodynamics.

Methods:

5D flow acquisition and reconstruction:

A previously described prototype free-running 5D flow sequence was implemented with balanced 4-point velocity encoding.[21,27,28] As shown in Figure 1A, a continuous scan following a 3D radial, spiral phyllotaxis sampling pattern,[28] delineated in 3D spherical coordinates with

$$r = constant$$

$$\varphi_n = \frac{2\pi}{360} n\, \varphi_{gold}$$

$$\theta_n = \frac{\pi}{2}\sqrt{\frac{n}{N}},$$

where r is the radius, φ_n the azimuthal angle, φ_{gold}=137.51°, θ_n the polar angle, and n=1,2,…
N increases with each readout. This pattern was segmented into multiple interleaves, each
initiated with a superior-inferior (SI) projection for self-gating. The 5D flow imaging
protocol used in this study was similar to a previous study,[26,29] where each interleaf
consisted of 6 total radial k-space trajectory angles corresponding to 21 total readouts (1 SI
projection + 5*[4 velocity encodes]). Sequential interleaves were rotated by the golden angle
(137.51°) throughout the entire scan.[30] All scans were acquired on a 1.5 T MAGNETOM
Aera (Siemens Healthcare, Erlangen, Germany).

Cardiac and respiratory motion signals were extracted from SI projections using a previously
validated principal component analysis (PCA) approach.[21,26,30-32] Using a chosen temporal
resolution of ~40 ms (temporal resolution = 8*repetition time TR), cardiac signals were used
to bin the acquired k-space lines into the appropriate cardiac time frame. Each line was also
tagged with the length of the heartbeat, RR_{Length}, within which it was acquired (Figure 1B,
C). All data were binned and reconstructed using the following two strategies:

Respiratory-Resolved 5D Reconstruction.—Prior 5D flow methods focus on
resolving respiration as the 5th dimension.[18,19,21,23,27] This respiratory-resolved
reconstruction scheme was based on strategies reported in a number of prior studies.[21,27,28]
Data were binned into a cardiac timepoint- and respiratory-resolved 5D flow data set (kx-ky-
kz-flow-cardiac-**respiration**). Four respiratory bins covering the full breathing cycle from
end-inspiration to end-expiration were used for all in vivo acquisitions. All data were
reconstructed using a previously described 5D flow framework by solving the following
optimization problem[21,27,32]:

$$m = arg\min_m \|FCm - s\|_2^2 + \lambda_c\| \nabla_c m\|_1 + \lambda_r \| \nabla_r m\|_1 + \lambda_\sigma\| \nabla_\sigma m\|_1$$

where m is the reconstructed 5D flow dataset, F is the non-uniform Fast Fourier Transform
operator, s, the acquired radial data, λ_c, λ_r and λ_σ the regularization weights along the
cardiac, respiratory, and spatial (x,y,z) dimensions, and ∇ the finite difference operator. λ_c =
0.0075, λ_σ = 0.0015, and λ_r = 0.005 were used for all reconstructions. These weights were
empirically determined based on previous studies in CS-accelerated 4D flow MRI and 5D
MRI.[21,26,27] Respiratory bins were divided such that the same number of radial k-space
views were mapped in each bin. The 5D respiration-resolved reconstruction resulted in four

reconstructed 4D flow datasets (3D + time), each corresponding to a different respiratory phase.

RR-Resolved 5D reconstruction.—Data were binned into a cardiac timepoint- and RR_{Length}-resolved 5D datasets (kx-ky-kz-flow-cardiac-**RR interval**) with 4 RR-interval bins. This reconstruction was not resolved for respiratory motion to ensure sufficient data per bin for the CS reconstruction. As a result, respiratory motion will cause some blurring artifacts in the reconstructed images.

For each patient, all unique $RR_{Lengths}$ were examined in order to determine 4 non-overlapping RR_{Length} bins, where each bin had the same number of RR-intervals (Figure 1C). Cardiac time frames with <300 radial views were rejected and truncated from the reconstruction. Because the temporal resolution was kept constant in each RR_{Length} bin, shorter RR intervals had inherently fewer cardiac phases than longer RR bins. The RR-resolved reconstruction, however, requires an equal number of cardiac phases in each bin for matrix-based data reconstruction. Thus, the last phase of shorter RR bins (RR1-3) was repeated so that all RR bins had the same number of cardiac timepoints as the longest bin (RR4). These repeated bins were then truncated to the proper RR lengths for dicom creation and image analysis.

The RR-Resolved reconstruction problem was as follows:

$$m = arg\min_m \|FCm - s\|_2^2 + \lambda_c \| \nabla_c m\|_1 + \lambda_{rr} \| \nabla_{rr} m\|_1 + \lambda_\sigma \| \nabla_\sigma m\|_1,$$

where λ_{rr} was the RR-interval regularization weight. In accordance with the respiratory-resolved 5D reconstruction, $\lambda_c = 0.0075$, $\lambda_\sigma = 0.0015$, and $\lambda_{rr} = 0.005$. The 5D RR-resolved reconstruction resulted in four reconstructed 4D flow datasets (3D + time), each corresponding to a different RR_{Length} range.

In vitro flow phantom experiments:

An MRI-compatible pulsatile flow circuit was used to simulate blood flow with arrhythmic beat-to-beat variation (Figure 2). Pulsatile flow was generated using a pneumatically-driven ventricular assist device (VAD) driven by a pressure pump control unit (MEDOS, Germany). The pumping action of the VAD was generated by a membrane sealed with water and the fluid circuit on one side, and air continuous with pneumatic tubing and the pump control unit on the other. When the volume of air on the pneumatic side increased, the membrane displacement drove fluid through the flow circuit. The VAD was placed in the scanner such that the periodic membrane movement was orthogonal to the table. An in-house LabVIEW (National Instruments, Austin, Texas, USA) program (Figure 2A) was used to send signals corresponding to user defined heart rates to the pump control unit and the MRI scanner (as a gating signal). The selection of arrhythmic heart rates was based on the mean in vivo RR-intervals measured in a prior pilot study in 12 AF patients.[33] The arrhythmic pulsatile flow experiment used a repeating sequence of VAD pump cycles with 68 bpm (RR_{Length} = 882 ms) for 10 beats, 86 bpm (RR_{Length} = 698 ms) for 6 beats, 46 bpm (RR_{Length} = 1304 ms) for 4 beats, followed by 56 bpm (RR_{Length} = 1071 ms) for 7 beats. In addition, a 2nd pulsatile

flow experiment with constant (sinus-rhythm) VAD pump cycles was performed with RR_{Length}=1000 ms (60 bpm).

5D flow data were acquired in a coronal imaging volume placed over the VAD and its inflow and outflow of tubes (Figure 2C), which allowed SI projections to capture the motion of the VAD membrane for extraction of self-gating cardiac signals. 5D flow imaging parameters were as follows: 101220 radial views, velocity sensitivity (Venc) = 150 cm/s, field of view (FOV)=280×280×280 mm^3, TE/TR=2.93/4.70 ms, flip angle (FA)=15°, acquired matrix size=112×112×112, reconstructed temporal resolution = 37.6 ms. 5D flow data were reconstructed using the respiratory-resolved 5D and RR-resolved reconstructions. Because the pulsatile phantom could not simulate respiration, one respiratory bin was used in the respiratory-resolved 5D reconstruction, while 4 RR bins were used for the RR-Resolved reconstruction. For reference, a real-time (RT) EPI-based 2D phase contrast (PC) scan[34,35] was also acquired in an orthogonal axial cut through the VAD in- and out-flow tubes for 40 seconds of fixed scan time, corresponding to 40 heartbeats (GRAPPA R=3, echo train length=7, temp res: 53.5 ms, FA=15°, TE=2.34 ms, spatial res: 2.7×2.7×9.1 mm^3).

For the 2nd sinus-rhythm in vitro flow experiment, an additional clinical standard ECG-gated 2D PC MRI scan was acquired (GRAPPA R=2, temp res: 35.6 ms, FA=20°, TE=2.34 ms, BW=455, spatial res: 2.1×2.1×7.0 mm^3) at the same 2D plane location.

All MRI acquisitions were repeated with flow turned off in order to collect background phase correction data.

In vitro data analysis:

The RR-Resolved 5D reconstruction resulted in four distinct in-vitro datasets (3D + time + 3-directional velocities), each corresponding to one of the four different RR-interval durations. Pre-processing of each of the in vitro 5D flow data included noise filtering and background phase correction by subtraction of the "flow-off" data from their corresponding "flow-on" scans. In addition, 5D flow pre-processing included calculation of a 3D phase-contrast MR angiogram (3D PC-MRA), which was used to segment the pipe sections of interest for flow quantification (VAD outflow tube, Figure 2C, red arrow). A 2D analysis plane was placed at the location of the 2D RT and standard PC acquisitions for calculation of time-resolved flow curves, and net and peak flows.

For analysis of the RT-PC data, an ROI was drawn over the phantom tube cross section to generate consecutive time-resolved flow curves over the 40 heartbeats (Figure 2D). A local minima approach was employed to identify the beginning of each "heartbeat" and to assign an RR_{Length} to each beat (Figure 2D). Each RT-PC heartbeat was assigned to one of the 4 RR-interval bins used for 5D reconstruction (RR1-RR4). Because RT data was acquired for many heartbeats, time-resolved flow data for the binned RT data (four RR1-RR4 bins) were interpolated to 50 time points and averaged to calculate a single flow curve that can be directly compared to the RR-resolved 5D flow data. Net and peak flows were calculated from each of these averaged flow waveforms.

In vivo study cohort:

25 adult patients (Age: 68.0±8.0 years; 6 females) with a previous history of AF were prospectively recruited for a non-contrast whole-heart 5D flow research MRI from June 2019 to March 2020. Relevant demographics and AF details are in Table 1. Eight patients had a history of cerebrovascular event. 5D flow imaging parameters matched those of the in vitro protocol, but with a flip angle of 7°, Venc = 100 cm/s, FOV=250×250×250 mm^3, matrix size=96×96×96, voxel size=2.5 mm^3 and a transverse imaging volume to capture superior-inferior respiratory motion. This HIPPA-compliant study was approved by our local Institutional Review Board and all patients provided written informed consent.

In vivo data analysis: Cardiac self-gating signals were used to calculate a measure of AF burden, where

$$AF\ Burden = \frac{IQR\ all\ RR}{Median\ all\ RR} \times 100,$$

and IQR represents the interquartile range.

A relatively large AF burden would suggest a wider range of intrascan heartrates and thus increased incidence of arrhythmias compared to a relatively low AF burden. Correlation analyses between AF Burden and hemodynamic parameters (PV, mean velocity, mean stasis) were performed. The results of these correlation analyses guided a sensitivity analysis to evaluate hemodynamic parameters (PV, stasis, and mean velocity) from 0.1 to 20% AF Burden to determine the optimal threshold for separation of patients into groups with low and high AF burden.

5D flow data of all patients were reconstructed using both respiratory- and RR-resolved 5D methods (Figure 3B, E). Only end-expiratory data (single respiratory phase) was used for respiration-resolved reconstruction analyses. Data pre-processing included noise-filtering, 3D background phase correction using a second-order polynomial fit to identifiable static tissue, and correction for velocity aliasing. In all patients, a 3D PC-MRA was calculated, and the left atrium (LA) was segmented from an RR-Resolved 5D dataset (RR2, Figure 3C). This 3D LA segmentation was used across all 4 RR-Resolved 5D data (RR1-RR4) and the respiratory-resolved 5D flow data to calculate the averaged top 5% peak velocity (PV) and mean velocity of the LA. Velocity data were also used to create velocity histograms of the LA over the cardiac cycle. In addition, stasis, defined as[36]

$$\frac{\#\ cardiac\ time\ frames\ where\ velocity < 0.1m\ /\ s}{total\ \#\ cardiac\ time\ frames} \times 100,$$

was quantified for each voxel in the LA. The stasis values were then projected as a mean intensity projection onto a 2D plane for calculation of stasis maps (Figure 3C, F), and used to calculate a single mean LA stasis value for each patient.

Statistical analyses:

All hemodynamic parameters are reported as mean±standard deviation. Continuous variables were evaluated for parameter normality using a Lilliefors test, and a non-parametric rank sum or two-tailed unpaired t-test was accordingly used to evaluate differences between high and low AF Burden subgroups. Bonferroni correction to adjust for multiple comparisons was used when relevant. Differences between RR interval bins were evaluated using a linear mixed effects model with the subjects treated as a random effect or a non-parametric Friedman test, with a paired t-test or Wilcoxon signed rank test performed in the case of significance. Correlations between parameters was investigated using a Pearson correlation coefficient (Pearson's r) or non-parametric Spearman's rank-order coefficient (Spearman's ρ).

Results

In vitro 5D flow

Pulsatile phantom results are summarized in Figure 2, Figure 4, and Table 1. Figure 4 depicts the RR-interval histogram used to assign the radial k-space lines into 4 bins over non-overlapping RR_{Length} ranges. While a pre-determined sequence of four different heartrates was sent to the pump, inherent system delays resulted in a more varied distribution of RR-intervals that could also be seen on operator observation of the pumping membrane (Figure 4A). Nonetheless, the resultant AF burden in the in vitro arrhythmic experiment was 22.0%.

Figure 4 demonstrates that the RR-Resolved 5D flow reconstruction (dotted, bold lines) successfully recovered the flow waveforms characteristic of the corresponding RR intervals compared to the 2D RT-PC reference flow (solid, bold lines). In contrast, respiratory-resolved 5D flow data (orange lines) failed to capture the shapes of 2D RT-PC flow waveforms over any of the RR intervals. Notably, the RR-Resolved 5D reconstruction was able to recover the bimodal flow curve shape of the longest RR interval (RR4) seen in the 2D RT-PC reference. As summarized in Table 2, 5D flow data generally overestimated peak flow (12.0% to 25.0%) and net flow (26.5% to 71.3%) in comparison to 2D RT-PC but was in excellent agreement with the standard ECG-gated 2D PC MRI (net flow: +4.1%, peak flow: +0.9%) from the sinus-rhythm in vitro flow experiment.

In vivo 5D flow

AF Burden: 5D flow data were successfully acquired in all participants (scan time: 8:48 min). AF burden of most patients (16 patients, 64% of cohort) was <10% (Table 2, overall range 3.0%–57.2%). Nine patients were above the AF burden threshold and classified with "high AF burden" (AF burden=29.1%±17.5% [11.2%–57.2%]), while the remaining 16 patients had "low AF burden (AF burden=5.5±1.9% [3.0%–9.7%]). When AF burden over all patients was evaluated, correlation analyses revealed significant correlations between increasing AF burden and respiratory-resolved 5D flow parameters (reduced mean velocity: ρ=−0.68, reduced PV: ρ= −0.54, elevated mean stasis: ρ=0.75, p<0.01, Supporting Information: Figure S1), and preserved significance in RR3 and RR4 (Supporting

Information, Table S1) in the RR-resolved reconstruction, with insignificant relationships only between AF Burden and RR1, RR2 PV.

Sensitivity Analysis: Because correlation analyses revealed significant correlations between AF burden and 5D flow parameters in RR3, RR4, and respiratory-resolved 5D reconstruction, these three reconstruction sets (RR3, RR4, respiratory-resolved 5D) were thus used as the basis for the sensitivity analysis (Figure S2A-C). For peak velocity, sensitivity analyses determined that classifying AF patients as those with an AF burden above 9.7% was necessary to differentiate low and high AF burden (threshold RR3=9.7%, RR4=9.5%, Standard Recon=9.5%). Mean stasis analyses determined a threshold above 6.7% (RR3=5.8%, RR4=5.5%, respiratory-resolved=6.7%) and mean velocity above 7.8% (RR3=6.7%, RR4=5.5%, respiratory-resolved =7.8%). Thus, the highest threshold, AF Burden= 9.7%, was selected as the threshold above which patients would be assigned to the high AF burden group.

For simplicity in the presentation of results, for patients with a low AF Burden (i.e. likely in sinus rhythm during imaging), only the respiratory-resolved 5D flow reconstruction is presented in the subsequent figures, depicting comparisons between the low and high AF burden cohorts, while both the standard and RR-resolved reconstructions are presented for patients with a high AF burden, because they demonstrated more RR variability. Additional results can be found in the Supporting Information (Table S2)

Low Versus High AF Burden: Figure 5 depicts two representative patients with low and high AF burden. The RR_{Length} histogram of the high AF Burden patient (Figure 5A) covered a much wider range of potential $RR_{Lengths}$ with corresponding lower LA mean stasis levels (Figure 5D-H) compared to the patient with a low AF Burden (Figure 5C). The patient with high AF burden demonstrated similar hemodynamics in all RR-resolved stasis maps (Figure 5D-G), but increased stasis (white arrow) and leftward narrowing of the velocity histogram with increasing RR. Respiratory-resolved 5D flow analyses demonstrated that patients with high AF burden had significantly higher mean stasis and lower mean and peak velocity compared to patients with low AF burden (Figure 6, Table 3, mean stasis: 36% higher; mean velocity: 20% lower; PV: 28% lower, p<0.01). These relationships were preserved when comparing the high AF burden, RR-resolved results from each of the four RR bins to the respiratory-resolved 5D flow results of the low AF burden patients (Figure 6, Table 3, mean stasis: 36-42% higher; mean velocity: 20-30% lower; PV: 25-41% lower, p<0.01).

Among patients with high AF burden, RR2 had the highest number of radial views compared to other RR bins. RR2-derived mean stasis and mean velocity values were closest to respiratory-resolved 5D flow data (mean stasis: RR2=1.3±7.0%, mean velocity: RR2=0.2±6.5%, p>0.4). Friedman or mixed effect model analysis revealed no significant differences in evaluated hemodynamic parameters between RR bins in patients with high AF burden (PV: p=0.17, mean stasis: p=0.22, mean velocity: p=0.12). However, these results allude to trends in inter-RR bin relationships: RR4 had the furthest deviation from respiratory-resolved 5D results with increased mean stasis (7.6%±14.0%, p=0.10), decreased PV (−12.7±14.2%, p=0.09), and decreased mean velocity (−5.8±10.5%, p=0.15) over all

patients. RR3 also tended to have relatively increased mean stasis (5.4%±1.2%, p=0.08) and decreased mean velocity (−4.5%±6.8%, p=0.14).

Discussion

Here, we have developed and validated a free-running, highly accelerated, 5D flow framework for investigating the effects of RR_{Length} on LA hemodynamics in AF. We have demonstrated that (1) 5D flow with RR-interval binning can resolve hemodynamics associated with varying heartbeats in an in vitro pulsatile flow circuit; (2) RR-resolved 5D flow is feasible in vivo in patients with AF and enables calculation of measures of AF burden; (3) 5D flow MRI can detect differences between patients with low and high AF burden; (4) encouraging trends between RR intervals suggest the potential role of RR-resolved 5D flow in investigating the effects or different RR-intervals on LA flow dynamics, and their relationship to thrombosis and stroke.

In vitro results validated the RR-resolved 5D flow framework in a controlled environment. While a pre-determined sequence of four different heartrates was sent to the pump, inherent and somewhat unpredictable mechanical latency of the pump resulted in a different set of resultant heartrates, with five rather than 4 peaks in the histogram. While the programmed sequence was thus not the intended "ground truth", the previously validated self-gating component[21,37] of the framework was used to track pump membrane movement, and RR-resolved 5D flow was able to recover RR_{Length}-driven flow waveform shapes that were not captured by the respiratory-resolved 5D reconstruction. The peak and net flow tended to be overestimated by RR-resolved 5D flow compared to the RT 2D-PC "reference standard". This RT sequence was previously shown to underestimate peak flows and velocities in vivo, likely due to the lower available spatial resolution, EPI readout, and use of view sharing.[34] Consequently, a non-arrhythmic (sinus) experiment was acquired as well, demonstrating agreement of 5D flow and clinical ECG-gated 2D PC-derived parameters. In addition, the 5D and 2D scans were acquired for different lengths of time, and thus the exact number of heartbeats in each RR bin in the RT scan was lower than in the 5D scan (40 seconds scan time versus ~ 9 minutes). However, the RT-PC sequence scan time was set so that the entire cyclic sequence of arrhythmic was played out at least once fully.

In vivo results further demonstrated the feasibility of the pipeline and revealed differences in left atrial flow and stasis for different arrhythmic RR interval durations. While stasis maps and LA hemodynamics revealed some trends, differences were not statistically significant. Among all RR bins, RR4, the longest bin, had more thromboembolic hemodynamic parameters (lower peak velocities, higher mean stasis) compared to the respiratory-resolved 5D reconstruction. These results suggest that typical, ECG-gated 4D flow techniques are able to capture the major features of LA hemodynamics, but may miss increased thromboembolic risk that may be associated with longer heartbeats.

Prior 4D flow studies have primarily focused on patients with a history of AF who were in sinus rhythm during imaging[38,39], or alternatively on using a binary system and categorizing patients into "in AF" or "in Sinus" at the time of imaging based on the ECG display at the MRI scanner.[40] These prior studies have demonstrated that patients in AF during imaging

exhibited significantly altered left atrial hemodynamics (increased stasis, decreased velocities) associated with thrombotic risk, compared to patients in sinus rhythm during imaging. However, most of these studies neglected to accommodate for arrhythmias in the acquisition protocol. Alternatively, many studies used arrhythmia rejection, where arrhythmic beats were rejected and reacquired, leading to decreased scan efficiency and less predictable scan times. The 5D flow MRI technique evaluated in this study was able to simultaneously explore the influence of arrhythmias while also reaffirming the results of prior studies within a predictable scan time. Specifically, 5D flow found that patients with high AF burden during imaging have significantly higher mean stasis, and significantly lower mean and peak velocities compared to those with a low AF burden. While these results were confirmed with the respiratory-resolved 5D flow reconstruction, this study aimed to introduce an approach that enables initial investigation of RR-influenced hemodynamics. Future studies incorporating larger varieties of AF presentation may further investigate the true influence, be it small or large, of arrhythmia on 3D hemodynamics.

In vivo results further demonstrated the utility of calculating 5D flow acquisition-derived AF burden for all patients, by identifying relationships between hemodynamic variables and continuous AF burden. The American Heart Association (AHA) has begun to advocate for the classification of AF not as a binary entity, but rather based on AF burden, a continuous variable representing the proportion of time that the patients are in AF.[11] Longitudinal studies have found that patients with persistent AF (high AF burden) are not only at higher risk of stroke than those with paroxysmal AF, but these patients have also had poorer neurological outcomes after cardioembolic stroke.[41-43] While the AHA mentions that AF burden is typically calculated from an electrophysiological monitor over a period of minutes to days, our technique was nonetheless able to calculate a relative measure of AF burden that was potentially significantly correlated with the severity of thromboembolic hemodynamic parameters (i.e. increasing stasis with increasing hemodynamic burden). Piekarski et al. previously reported a similar measure of self-gating signal that could separate non-arrhythmic patients from arrhythmic patients.[37] While Piekarski does not report an AF Burden threshold for low versus high AF burden, their results suggest a threshold of just under 17.0%, a value that is close to the AF burden of the least arrhythmic patient with persistent AF (Table 1, subject 19). We investigated splitting patients into groups of persistent/permanent AF versus paroxysmal AF (PAF), and found it preserved the hemodynamic relationships seen between low and high AF burden. However, the relationships between *persistent RR2 and Resp-Resolved* reconstructions versus *PAF Resp-Resolved* were no longer statistically significant ($p = 0.1$, $p=0.05$, respectively), potentially due to the smaller sample size (n=6, persistent). Piekarski was also limited by small sample sizes of 33 patients total, and only 6 with AF, and thus larger studies are still needed to investigate the true threshold over different measures of AF burden. In addition, without constant monitoring of patients, PAF is often difficult to classify fully accurately in all patients, especially in small sample sizes. Future studies will ideally include a Holter/ continuous monitoring device to use the ECG waveform to more accurately quantify the percent of time spent in AF over a period of at least 24 hours.

This study was primarily limited by the small sample size and lack of RT in vivo validation. The lack of an in vivo reference standard made it difficult to fully validate the in vivo

application of this technique. This will be an ongoing challenge, as real-time data are operator-dependent, and often difficult to place in the same relative area across patients in intracardiac imaging (i.e. LA). Moreover, as mentioned previously, RT techniques have limitations in themselves. These differences will be better explored with larger study cohorts.

Accordingly, AF can present along a continuous spectrum of potential $RR_{Lengths}$, and the majority of the patients in this study had a low AF burden. This study initially considered binning data into bins with equal numbers of projections, while maintaining the temporal resolution across RR bins for more accurate comparisons of inter-bin stasis. This approach likely would have further improved the performance of the TV-based reconstruction, especially in the RR-interval dimension, where relatively low regularization weights were used. However, the wide range of RR intervals in histograms of patients with a high AF burden demonstrate that the majority of the scan is spent in a narrower range of heartrates, and that equal bin sizes would have inevitably caused overflow of the hemodynamics that are more representative of the "average" heartrate into the more "arrhythmic" bins in patients with high AF burden. Moreover, the weights used in this study were based on previous 5D flow studies with similar dimensionality. Long reconstruction times for multi-dimensional CS reconstruction, and the need to determine robust reconstruction weights are well known limitations of accelerated imaging studies. Future studies will further exploration of robust regularization weights, and incorporate longer scan times over a wide variety of AF burden presentations to identify a binning strategy that works best for all AF patients, or alternatively, may suggest that patients with higher AF burden should be binned and investigated differently from those with low AF burden. Further investigations of data uniformity in this study are included in the supplemental information (Supporting Information: Figure S3). Nonetheless, this preliminary study demonstrated the sensitivity of this 5D flow framework to RR_{Length}-driven hemodynamic differences, and was able to identify an AF burden threshold that was sensitive to differences between high and low burden groups.

In addition, radial 5D flow with compressed sensing reconstruction, as used in this study, is currently still limited by long reconstruction times, on the order of 5 to 15 hours, depending on the size of the dataset. However, compressed sensing reconstruction times have been decreasing with increasingly advanced hardware and vendor support as well as improvements in the field of AI-based image reconstruction.[44-47] In addition, the respiratory-resolved 5D flow reconstruction undersamples data to <3% of Nyquist, and thus to prevent further data dilution and keep the same number of dimensions, the RR binning dimension was not used concurrently with a respiratory dimension. This likely caused some blurring of the LA for a more difficult segmentation. However, 3D radial imaging is inherently relatively robust to motion, and thus the LA was still identifiable in all patients. In addition, the last bin of shorter RR bins needed to be duplicated to match the number of cardiac timepoints along the RR-interval dimension for the CS reconstruction. This solution is potentially suboptimal and may have introduced undesired artifacts. Cardiac bins with fewer than 300 radial views were also truncated to prevent further dilution when split into RR and respiratory bins. This primarily affected the longest RR bins, however, initial patients verified that flow waveforms did not demonstrate truncation over the cardiac cycle.

Further binning investigations could also include weighting of quantified parameters (stasis, velocities) by the relative number of k-space lines in each RR bin, as well as testing using multiple in vitro arrhythmic experiments with a variety of arrhythmic sequences. This weighting could potentially account for the relative effects of the amount of time spent in short or long RR intervals. In addition, future studies will include a longer acquisition protocol to expand the 5D flow framework dimensionality, with cardiac timepoint, RR_{Length} or alternative arrhythmia measures,[48] and respiration concurrently resolved, and potential respiratory motion compensation for reduction of motion blurring.

In conclusion, we have demonstrated the feasibility of a <10 minute, whole-heart scan within a novel RR-based 5D flow framework to investigate arrhythmia-resolved reconstruction of 3D hemodynamics. With larger cohorts, RR-resolved 5D flow MRI may further discern the true effects of RR interval on hemodynamics in AF, as well as provide a more efficient alternative for imaging complex arrhythmic patients.

Supplementary Material

Refer to Web version on PubMed Central for supplementary material.

Acknowledgements:

References

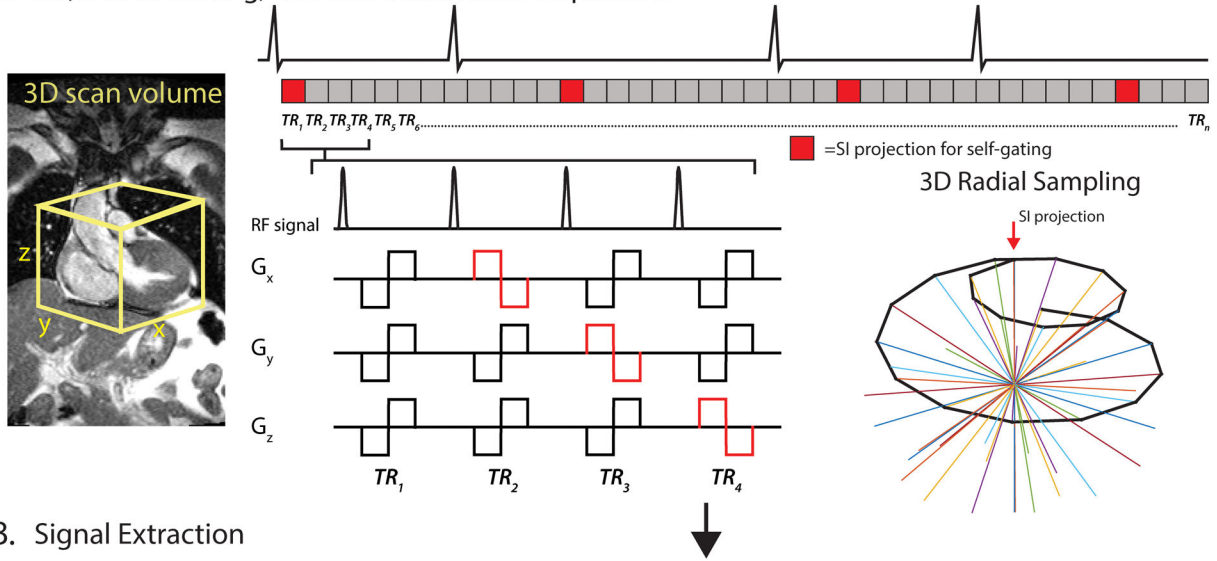1. Chugh SS, Havmoeller R, Narayanan K, et al. Worldwide epidemiology of atrial fibrillation: a Global Burden of Disease 2010 Study. Circulation. 2014;129(8):837–847. [PubMed: 24345399]

2. Fibrillation A Prevalence of diagnosed atrial fibrillation in adults. Jama. 2001;285:2370–2375. [PubMed: 11343485]

3. January CT, Wann LS, Alpert JS, et al. 2014 AHA/ACC/HRS Guideline for the Management of Patients With Atrial FibrillationA Report of the American College of Cardiology/American Heart Association Task Force on Practice Guidelines and the Heart Rhythm Society. Journal of the American College of Cardiology. 2014;64(21):e1–e76. [PubMed: 24685669]

4. Miyasaka. Secular trends in incidence of atrial fibrillation in Olmsted County, Minnesota, 1980 to 2000, and implications on the projections for future prevalence (vol 114, pg 119, 2006). Circulation. 2006;114(11):E498–E498.

5. Iwasaki Y-k, Nishida K, Kato T, Nattel S. Atrial fibrillation pathophysiology: implications for management. Circulation. 2011;124(20):2264–2274. [PubMed: 22083148]

6. Israel C, Kitsiou A, Kalyani M, et al. Detection of atrial fibrillation in patients with embolic stroke of undetermined source by prolonged monitoring with implantable loop recorders. Thrombosis and haemostasis. 2017;117(10):1962–1969. [PubMed: 28862284]

7. Pollick C, Taylor D. Assessment of left atrial appendage function by transesophageal echocardiography. Implications for the development of thrombus. Circulation. 1991;84(1):223–231. [PubMed: 2060098]

8. Cibis M, Lindahl TL, Ebbers T, Karlsson LO, Carlhäll C-J. Left atrial 4D blood flow dynamics and hemostasis following electrical cardioversion of atrial fibrillation. Frontiers in physiology. 2017;8:1052. [PubMed: 29311980]

9. Fluckiger JU, Goldberger JJ, Lee DC, et al. Left atrial flow velocity distribution and flow coherence using four-dimensional FLOW MRI: A pilot study investigating the impact of age and Pre-and

Postintervention atrial fibrillation on atrial hemodynamics. Journal of Magnetic Resonance Imaging. 2013;38(3):580–587. [PubMed: 23292793]

10. Lee DC, Markl M, Ng J, et al. Three-dimensional left atrial blood flow characteristics in patients with atrial fibrillation assessed by 4D flow CMR. European Journal of Echocardiography. 2015;17(11):1259–1268.

11. Chen LY, Chung MK, Allen LA, et al. Atrial fibrillation burden: moving beyond atrial fibrillation as a binary entity: a scientific statement from the American Heart Association. Circulation. 2018;137(20):e623–e644. [PubMed: 29661944]

12. Markl M, Lee DC, Furiasse N, et al. Left atrial and left atrial appendage 4D blood flow dynamics in atrial fibrillation. Circulation: Cardiovascular Imaging. 2016;9(9):e004984. [PubMed: 27613699]

13. Markl M, Lee DC, Ng J, Carr M, Carr J, Goldberger JJ. Left atrial 4d flow mri: stasis and velocity mapping in patients with atrial fibrillation. Investigative radiology. 2016;51(3):147. [PubMed: 26488375]

14. Christodoulou AG, Shaw JL, Nguyen C, et al. Magnetic resonance multitasking for motion-resolved quantitative cardiovascular imaging. Nature biomedical engineering. 2018;2(4):215–226.

15. Hu Z, Christodoulou AG, Wang N, et al. Magnetic resonance multitasking for multidimensional assessment of cardiovascular system: Development and feasibility study on the thoracic aorta. Magnetic Resonance in Medicine. 2020.

16. Jaubert O, Cruz G, Bustin A, et al. Free-running cardiac magnetic resonance fingerprinting: Joint T1/T2 map and Cine imaging. Magnetic resonance imaging. 2020;68:173–182. [PubMed: 32061964]

17. Qi H, Bustin A, Kuestner T, et al. Respiratory motion-compensated high-resolution 3D whole-heart T1ρ mapping. Journal of Cardiovascular Magnetic Resonance. 2020;22(1):12. [PubMed: 32014001]

18. Bastiaansen JA, Piccini D, Di Sopra L, et al. Natively fat-suppressed 5D whole-heart MRI with a radial free-running fast-interrupted steady-state (FISS) sequence at 1.5 T and 3T. Magnetic resonance in medicine. 2019.

19. Bastkowski R, Bindermann R, Brockmeier K, Weiss K, Maintz D, Giese D. Respiration Dependency of Caval Blood Flow in Patients with Fontan Circulation: Quantification Using 5D Flow MRI. Radiology: Cardiothoracic Imaging. 2019;1(4):e190005.

20. Bastkowski R, Weiss K, Maintz D, Giese D. Self-gated golden-angle spiral 4D flow MRI. Magnetic resonance in medicine. 2018;80(3):904–913. [PubMed: 29344990]

21. Di Sopra L, Piccini D, Coppo S, Stuber M, Yerly J. An automated approach to fully self-gated free-running cardiac and respiratory motion-resolved 5D whole-heart MRI. Magnetic resonance in medicine. 2019;82(6):2118–2132. [PubMed: 31321816]

22. Schrauben EM, Lim JM, Goolaub DS, Marini D, Seed M, Macgowan CK. Motion robust respiratory-resolved 3D radial flow MRI and its application in neonatal congenital heart disease. Magnetic resonance in medicine. 2019.

23. Walheim J, Dillinger H, Kozerke S. Multipoint 5D flow cardiovascular magnetic resonance-accelerated cardiac-and respiratory-motion resolved mapping of mean and turbulent velocities. Journal of Cardiovascular Magnetic Resonance. 2019;21(1):42. [PubMed: 31331353]

24. Cheng JY, Zhang T, Alley MT, et al. Comprehensive multi-dimensional MRI for the simultaneous assessment of cardiopulmonary anatomy and physiology. Scientific reports. 2017;7(1):1–15. [PubMed: 28127051]

25. Ma L, Yerly J, Di Sopra L, et al. 5D flow MRI: A Free-running, fully self-gated, radial imaging framework for cardiac and respiratory motion-resolved assessment of 3D blood flow dynamics Paper presented at: Proc. Intl. Soc. Mag. Reson. Med 27 2019; Montreal, Canada.

26. Ma L, Yerly J, Piccini D, et al. 5D Flow MRI: A Fully Self-gated, Free-running Framework for Cardiac and Respiratory Motion–resolved 3D Hemodynamics. Radiology: Cardiothoracic Imaging. 2020;2(6).

27. Feng L, Coppo S, Piccini D, et al. 5D whole-heart sparse MRI. Magnetic resonance in medicine. 2018;79(2):826–838. [PubMed: 28497486]
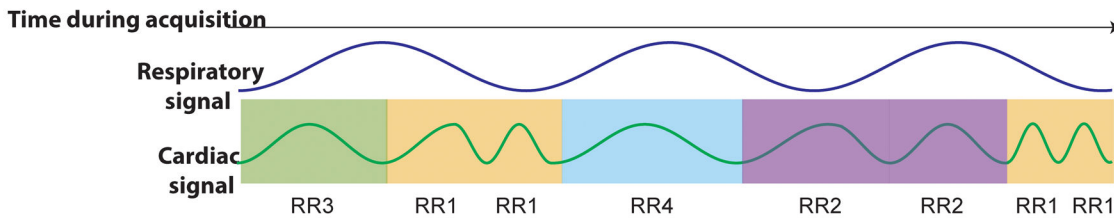
28. Piccini D, Littmann A, Nielles-Vallespin S, Zenge MO. Spiral phyllotaxis: the natural way to construct a 3D radial trajectory in MRI. Magnetic resonance in medicine. 2011;66(4):1049–1056. [PubMed: 21469185]

29. Ma LE, Yerly J, Roy CW, et al. 5D flow MRI: A Free-running, fully self-gated, radial imaging framework for cardiac and respiratory motion-resolved assessment of 3D blood flow dynamics Proc of the International Society for Magnetic Resonance in Medicine; 5 11–17, 2019; Montreal, Canada. 2019.

30. Pang J, Sharif B, Fan Z, et al. ECG and navigator-free four-dimensional whole-heart coronary MRA for simultaneous visualization of cardiac anatomy and function. Magnetic resonance in medicine. 2014;72(5):1208–1217. [PubMed: 25216287]

31. Chandarana H, Feng L, Ream J, et al. Respiratory motion-resolved compressed sensing reconstruction of free-breathing radial acquisition for dynamic liver MRI. Investigative radiology. 2015;50(11):749. [PubMed: 26146869]

32. Feng L, Axel L, Chandarana H, Block KT, Sodickson DK, Otazo R. XD-GRASP: golden-angle radial MRI with reconstruction of extra motion-state dimensions using compressed sensing. Magnetic resonance in medicine. 2016;75(2):775–788. [PubMed: 25809847]

33. Ma L, Yerly J, Di Sopra L, et al. Decoding the Effects of Rhythm on Hemodynamics in Patients with Atrial Fibrillation Using a 5D Flow Framework. Paper presented at: Annual Meeting of the International Society for Magnetic Resonance Imaging in Medicine 2020; Paris, France.

34. Traber J, Wurche L, Dieringer MA, et al. Real-time phase contrast magnetic resonance imaging for assessment of haemodynamics: from phantom to patients. European radiology. 2016;26(4):986–996. [PubMed: 26188655]

35. Lin HY, Bender JA, Ding Y, et al. Shared velocity encoding: a method to improve the temporal resolution of phase-contrast velocity measurements. Magnetic resonance in medicine. 2012;68(3):703–710. [PubMed: 22139889]

36. Markl M, Lee DC, Ng J, Carr M, Carr J, Goldberger JJ. Left Atrial 4-Dimensional Flow Magnetic Resonance Imaging: Stasis and Velocity Mapping in Patients With Atrial Fibrillation. Investigative radiology. 2016;51(3):147–154. [PubMed: 26488375]

37. Piekarski E, Chitiboi T, Ramb R, Feng L, Axel L. Use of self-gated radial cardiovascular magnetic resonance to detect and classify arrhythmias (atrial fibrillation and premature ventricular contraction). Journal of Cardiovascular Magnetic Resonance. 2017;18(1):83.

38. Garcia J, Sheitt H, Bristow MS, et al. Left atrial vortex size and velocity distributions by 4D flow MRI in patients with paroxysmal atrial fibrillation: Associations with age and CHA2DS2-VASc risk score. Journal of Magnetic Resonance Imaging. 2020;51(3):871–884. [PubMed: 31334898]

39. Karlsson LO, Erixon H, Ebbers T, Bolger A, Carlhäll C-J. Post-cardioversion improvement in LV function defined by 4D flow patterns and energetics in patients with atrial fibrillation. Frontiers in physiology. 2019;10:659. [PubMed: 31191353]

40. Cibis M, Lindahl TL, Ebbers T, Karlsson LO, Carlhäll C-J. Left Atrial 4D Blood Flow Dynamics and Hemostasis following Electrical Cardioversion of Atrial Fibrillation. Frontiers in physiology. 2017;8:1052–1052. [PubMed: 29311980]

41. Deguchi I, Fukuoka T, Hayashi T, et al. Clinical outcomes of persistent and paroxysmal atrial fibrillation in patients with stroke. Journal of Stroke and Cerebrovascular Diseases. 2014;23(10):2840–2844. [PubMed: 25294056]

42. Deguchi I, Hayashi T, Fukuoka T, Kobayashi S, Tanahashi N, Group JSSRS. Features of cardioembolic stroke with persistent and paroxysmal atrial fibrillation–a study with the Japan Stroke Registry. European journal of neurology. 2015;22(8):1215–1219. [PubMed: 25962447]

43. Naess H, Waje-Andreassen U, Thomassen L. Persistent atrial fibrillation is associated with worse prognosis than paroxysmal atrial fibrillation in acute cerebral infarction. ISRN cardiology. 2012;2012.

44. Akçakaya M, Moeller S, Weingärtner S, U urbil K. Scan-specific robust artificial-neural-networks for k-space interpolation (RAKI) reconstruction: Database-free deep learning for fast imaging. Magnetic resonance in medicine. 2019;81(1):439–453. [PubMed: 30277269]

45. Fuin N, Bustin A, Küstner T, et al. A multi-scale variational neural network for accelerating motion-compensated whole-heart 3D coronary MR angiography. Magnetic resonance imaging. 2020.

46. Hammernik K, Klatzer T, Kobler E, et al. Learning a variational network for reconstruction of accelerated MRI data. Magnetic resonance in medicine. 2018;79(6):3055–3071. [PubMed: 29115689]

47. Mardani M, Gong E, Cheng JY, et al. Deep generative adversarial neural networks for compressive sensing MRI. IEEE transactions on medical imaging. 2018;38(1):167–179. [PubMed: 30040634]

48. Chitiboi T, Feng L, Ramb R, Otazo R, Axel L. Reconstruction of arrhythmic cardiac cycles in patients with atrial fibrillation Proceedings of the International Society for Magnetic Resonance in Medicine, Paris 2018.
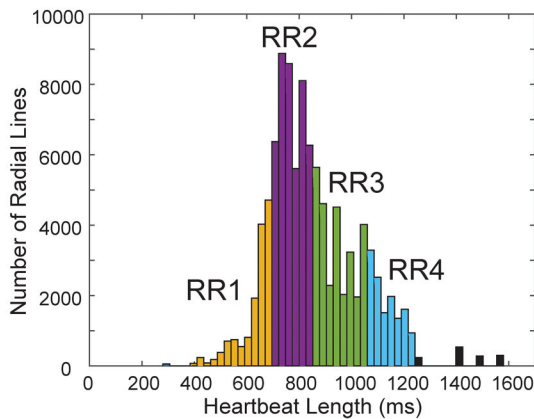
A. 3D, free breathing, ECG-less continuous acquisition

3D scan volume

=SI projection for self-gating

3D Radial Sampling

SI projection

RF signal

G_x

G_y

G_z

TR_1 TR_2 TR_3 TR_4

B. Signal Extraction

Time during acquisition

Respiratory signal

Cardiac signal

RR3 RR1 RR1 RR4 RR2 RR2 RR1 RR1

C. Assign heartbeat length (RR) to each line

RR2

RR3

RR4

RR1

Number of Radial Lines

Heartbeat Length (ms)

D. Multidimensional Data Binning

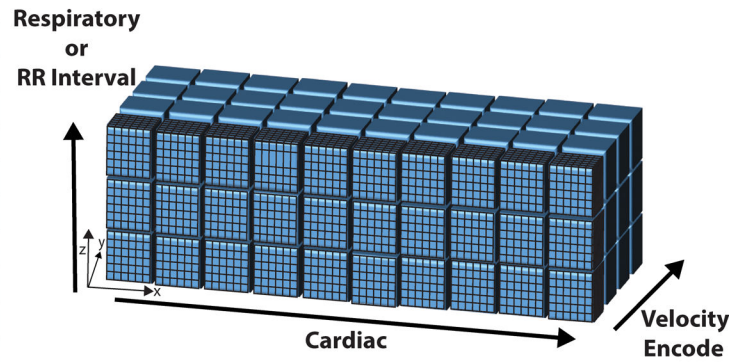Respiratory or RR Interval

Cardiac

Velocity Encode

Figure 1: 5D flow RR-binning framework.

A, a transverse, 3D radial imaging volume was placed over the heart. 4-point velocity encoding was combined with a 3D radial, spiral phyllotaxis, sampling pattern. A periodic superior-inferior (SI) projection started each interleaf (red blocks). B, the SI projections were used to extract cardiac and respiratory signals. Each heartbeat was additionally assigned a heartbeat length (RR_{Length}) and binned into one of four RR bins (RR1-RR4). C, histogram of RR intervals for a representative patient colored by bins corresponding to RR bins. Black bars represent outlier heartbeats with that were not included in the binning. D,

multidimensional reconstruction. ECG is shown for demonstration purposes only. Actual cardiac and RR binning were done via extracted SI projections. TR=repetition time.
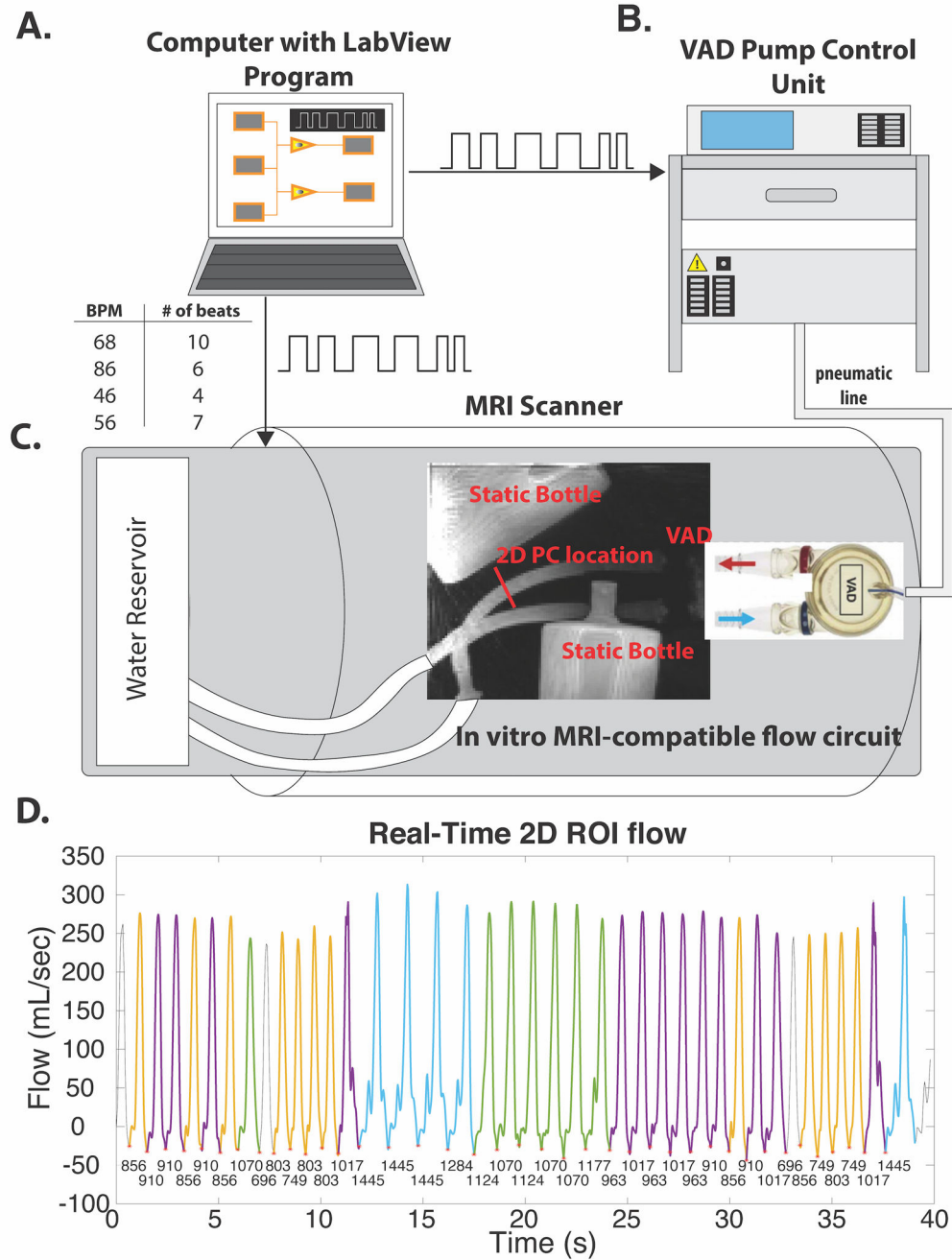
Figure 2: Pulsatile phantom.
A, computer with LabView program sends preprogrammed sequence of desired heartbeats to both the VAD pump control unit (B) and MRI scanner (C). The pump control unit drives the VAD from outside the scanner room by sending air through a pneumatic line. C, 5D flow imaging volume includes the ventricular assist device (VAD), which drives pulsatile flow through an air-water separating membrane that moves orthogonally to the inflow outflow tubes (in/out of the page). This VAD was included in the imaging volume to extract cardiac motion signals. D, RT 2D PC flow curve over the 40 second scan. RR intervals are under each cardiac trigger (red asterisks), each color corresponds to a different RR bin. Colors

correspond to RR interval bins in Figure 3. Three heartbeats (gray) were not within the range of any of the 5D flow RR bins, and thus not used for comparisons. VAD indicates pneumatically-driven ventricular assist device; BPM, beats per minute; ROI, region of interest.
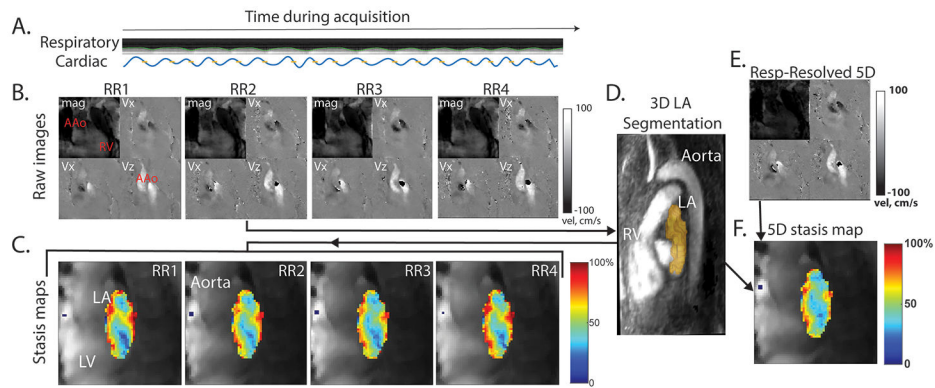
Figure 3: In vivo 5D flow analysis workflow.
A, representative respiratory and cardiac signals acquired from an AF patient. B, phase and magnitude images were reconstructed offline using both the respiratory-resolved 5D flow reconstruction (E) and the RR-Binned reconstruction (B) from continuously acquired raw data. A single RR-resolved reconstruction (RR2) was used to calculate a 3D PC-MRA for segmentation of the LA (C). This segmentation was applied to all RR datasets (RR1-RR4) as well as the Respiratory-resolved 5D reconstruction, for analysis of hemodynamic parameters, and visualization using mean stasis maps, where stasis is calculated for every voxel in the LA, and the mean stasis is projected onto a 2D plane (C, F). Note: some aliasing can be seen in the phase images, however, this is not in the volume of interest (LA) and was nonetheless corrected in pre-processing. AAo indicates ascending aorta; RV, right ventricle; LV, left ventricle; LA, left atrium.
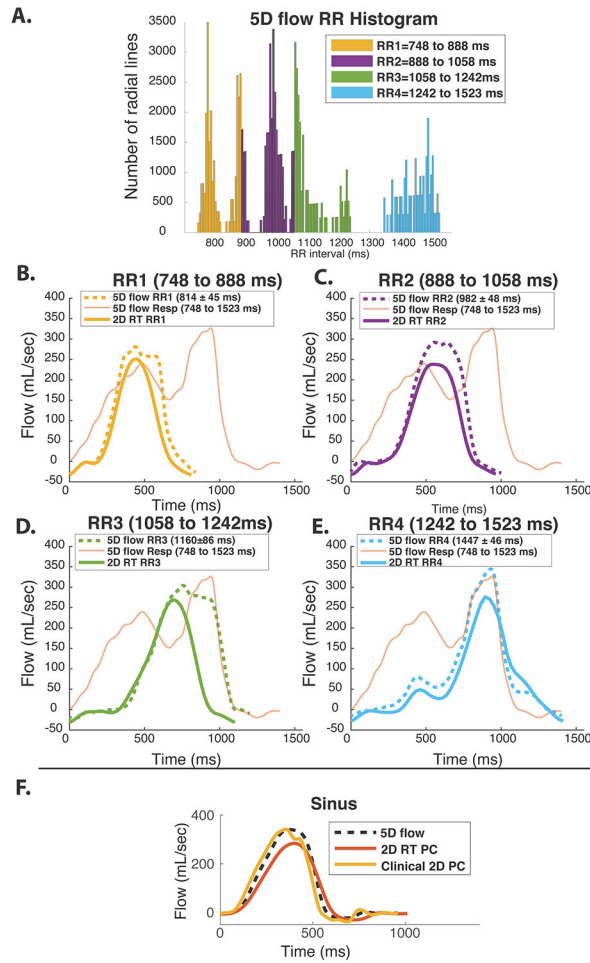
Figure 4: Flow waveforms of in vitro 2D RT and 5D flow.
A, histogram of RR-intervals during 5D flow scan with colors representing 4 RR bins (RR1-RR4) used for both 5D flow and RT flow analysis. B-E represent RR1 through RR4 for arrhythmic pulsatile experiment. RT colors correspond to the colors shown in Figure 2B. 5D flow curves from a planar location for each reconstructed RR-duration bin are delineated with dotted lines. The respiratory-resolved 5D flow reconstruction is overlaid over each plot (thin orange line). RR binning was able to recover the 5D flow waveforms (black line) corresponding to the real time scan while the respiratory-resolved 5D reconstruction did not match any RT flow curves. F, sinus experiment with RR=1000 ms demonstrates relative RT underestimation compared to the clinically respiratory-resolved ECG-gated 2D PC scan.
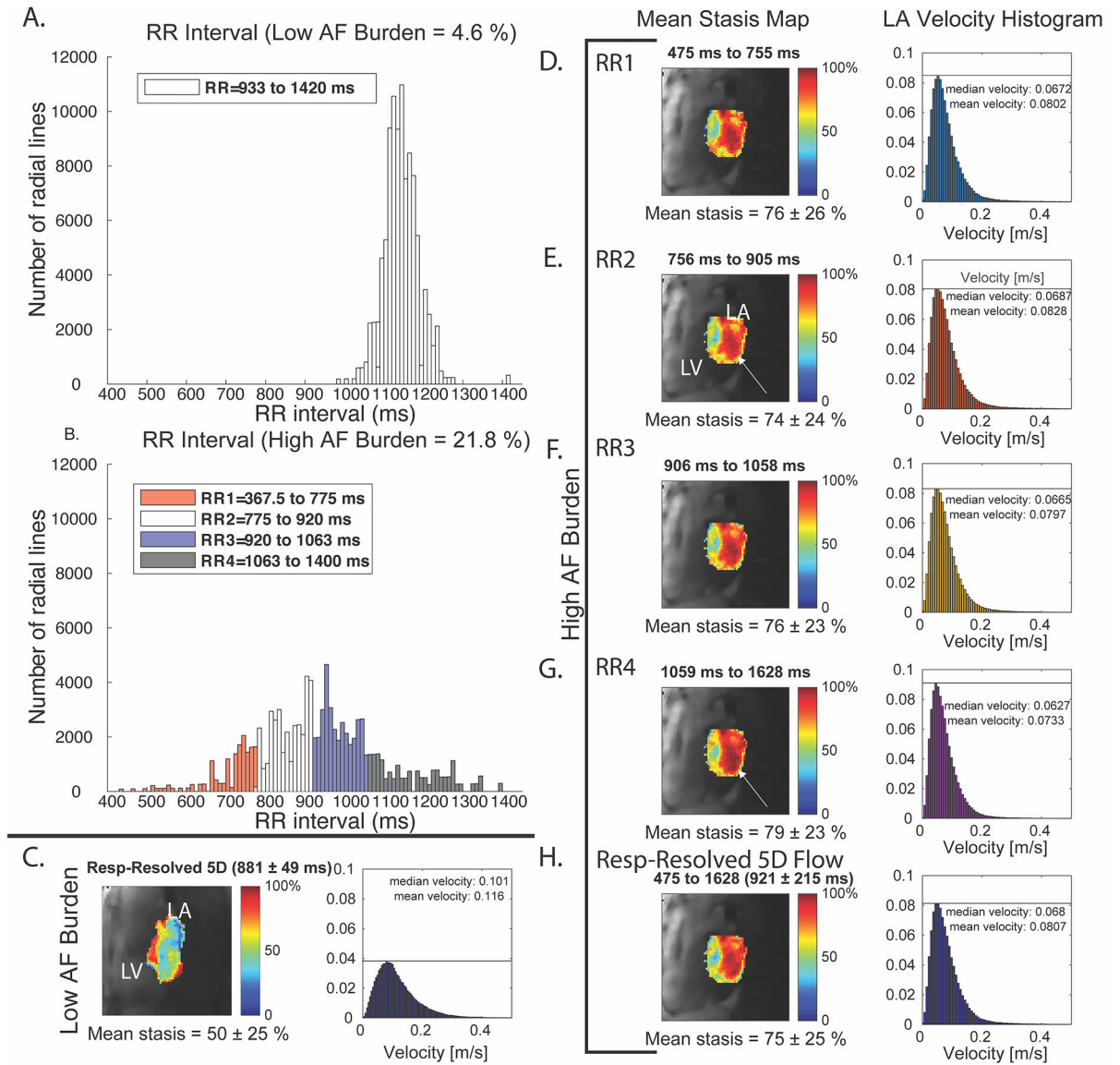
Figure 5: Example results from AF and sinus patient.
A, stasis maps and velocity histograms of the LA for a patient in AF. A, B, histogram with color-coded bins of low and high AF burden patients. B, patient with low AF burden during imaging shows much lower stasis and higher velocities compared to RR interval binned reconstruction of high AF burden patient (D-H). All high AF burden stasis maps appear similar (RR-binned and respiratory-resolved 5D reconstruction, with slight increases in stasis with longer RR_{Length} (white arrows).
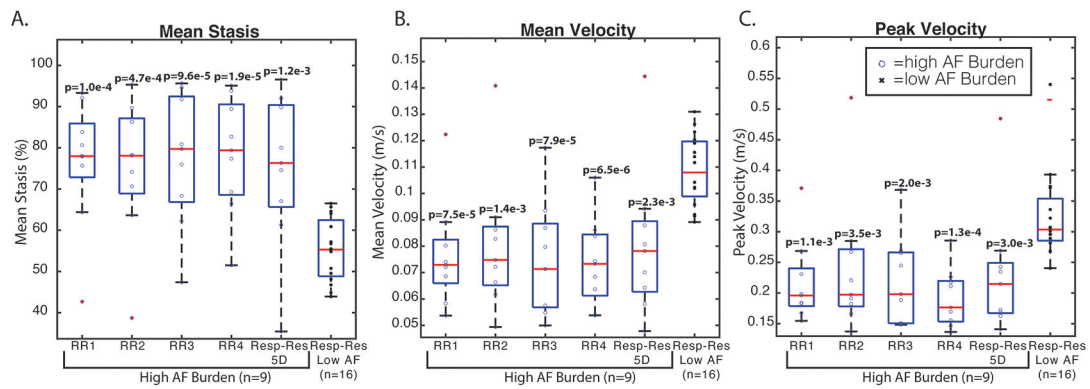
Figure 6: Box plots of patients with low vs. high AF burden.
The first five columns of each boxplot correspond to the RR-resolved and respiratory-resolved 5D reconstruction for high AF burden patients (n=9), while the last column corresponds to low AF burden (n=16). Patients with high AF burden (blue circles) had significantly higher mean stasis (A) and lower mean and peak velocities (B, C) in all RR bins and the respiratory-resolved 5D reconstruction ("respiratory-resolved") compared to patients with low AF burden during imaging (black x's). p values are indicative of comparison between high AF burden reconstructions compared to the respiratory-resolved 5D reconstruction for low AF burden patients.

Table 1:

Patient demographics.

AF history and demographic information for all 25 AF patients. PAF=paroxysmal AF.

Subject Number	Gender	Age at scan	CHA2DS2-VASc	History of stroke	AF History	AF Duration (years)	AF Burden	AF group
1	M	77.0	5	yes	PAF	7	3.0	low
2	M	76.3	4	yes	PAF	18	3.4	low
3	F	71.1	2	no	PAF	>5	4.3	low
4	F	63.3	2	no	PAF	5	4.5	low
5	F	61.6	2	no	PAF	4	4.5	low
6	M	52.8	0	no	PAF	>5	4.5	low
7	F	62.8	3	no	PAF	>5	4.6	low
8	M	57.4	0	no	PAF	2	4.6	low
9	M	67.5	3	yes	PAF	<1	4.9	low
10	M	74.9	2	no	PAF	>5	5.3	low
11	M	80.2	5	yes	PAF	>5	5.4	low
12	F	68.6	6	no	PAF	<1	5.8	low
13	M	53.2	1	no	PAF	2	6.7	low
14	M	68.8	7	yes	PAF	1	7.8	low
15	F	66.1	5	no	PAF	2	9.5	low
16	M	70.2	3	no	PAF	10	9.7	low
17	M	76.9	3	no	PAF	4	11.2	high
18	M	66.3	5	yes	PAF	>5	13.0	high
19	M	68.6	2	yes	Persistent	8	17.0	high
20	M	63.6	1	no	Persistent	3	19.9	high
21	M	69.2	3	no	Persistent	>8	21.8	high
22	M	70.3	1	no	Permanent	>20	27.7	high
23	M	56.4	0	no	PAF	>3	38.5	high
24	M	78.5	4	yes	Persistent	2	55.4	high
25	M	81.3	3	no	Permanent	unknown	57.2	high

Table 2:
In vitro flow parameters for 5D flow, 2D RT, and the clinically standard, ECG-gated 2D PC scan.

RR=1000 represents the sinus experiment.

5D flow					
	RR=1000 ms	*RR1=814±45 ms*	*RR2=982±48 ms*	*RR3=1160±86 ms*	*RR4=1147±46 ms*
Net flow (mL/cycle)	95	90	104	135	118
Peak flow (mL/s)	340	281	292	304	345
Real-time 2D PC averaged over RR range					
	RR=1000 ms	*RR1=749 to 856 ms*	*RR2=910 to 1017 ms*	*RR3=1070 to 1177 ms*	*RR=1284 to 1445 ms*
Net flow (mL/cycle)	78	62	74	79	94
Peak flow (mL/s)	284	251	238	269	276
Clinical, ECG-gated 2D PC					
Net flow (mL/cycle)	92				
Peak flow (mL/s)	337				

Table 3:

Low vs high AF burden hemodynamics and binning-related parameters.

The first three rows include scan- and binning-related parameters while the last three rows include quantified hemodynamic LA values. Respiratory-resolved 5D reconstructions were analyzed for all patients. For high AF burden patients, a RR-resolved reconstruction was included (columns RR1-RR4), along with relevant parameters for all RR bins.

	High AF Burden					Low AF Burden
	RR1	RR2	RR3	RR4	Respiratory-resolved 5D	Respiratory-resolved 5D
Mean RR interval (ms)	646±127 (532 to 962)	853±191 (656 to 1291)	1056±290 (771 to 1578)	1321±412 (960 to 2018)	968±245 (746 to 1460)	1011±91 (881 to 1163)
Bin Edges (ms)	330±89 to 760±154	761±154 to 941±222	942±222 to 1169±357	1170±357 to 1711±545	330±89 to 1711±545	613±230 to 1305±183
Number of radial views	12528±3172	30851±10041	32098±9721	20922±8350	101220	101220
Mean Stasis (%)	76±15	75±17	77±16	78±14	75±19	55±8
Peak Velocity (m/s)	0.22±0.07	0.24±.11	0.22±0.07	0.19±0.05	0.23±0.10	0.32±0.07
Mean Velocity (m/s)	0.08±0.02	0.08±0.03	0.08±0.02	0.07±0.02	0.08±0.03	0.10±0.01